PLANETARY SCIENCE

Seismic detection of the martian core

Simon C. Stähler[1]*, Amir Khan[1,2], W. Bruce Banerdt[3], Philippe Lognonné[4], Domenico Giardini[1], Savas Ceylan[1], Mélanie Drilleau[5], A. Cecilia Duran[1], Raphaël F. Garcia[5], Quancheng Huang[6], Doyeon Kim[6], Vedran Lekic[6], Henri Samuel[4], Martin Schimmel[7], Nicholas Schmerr[6], David Sollberger[1], Éléonore Stutzmann[4], Zongbo Xu[4], Daniele Antonangeli[8], Constantinos Charalambous[9], Paul M. Davis[10], Jessica C. E. Irving[11], Taichi Kawamura[4], Martin Knapmeyer[12], Ross Maguire[6], Angela G. Marusiak[3], Mark P. Panning[3], Clément Perrin[13], Ana-Catalina Plesa[12], Attilio Rivoldini[14], Cédric Schmelzbach[1], Géraldine Zenhäusern[1], Éric Beucler[13], John Clinton[15], Nikolaj Dahmen[1], Martin van Driel[1], Tamara Gudkova[16], Anna Horleston[11], W. Thomas Pike[9], Matthieu Plasman[4], Suzanne E. Smrekar[3]

Clues to a planet's geologic history are contained in its interior structure, particularly its core. We detected reflections of seismic waves from the core-mantle boundary of Mars using InSight seismic data and inverted these together with geodetic data to constrain the radius of the liquid metal core to 1830 ± 40 kilometers. The large core implies a martian mantle mineralogically similar to the terrestrial upper mantle and transition zone but differing from Earth by not having a bridgmanite-dominated lower mantle. We inferred a mean core density of 5.7 to 6.3 grams per cubic centimeter, which requires a substantial complement of light elements dissolved in the iron-nickel core. The seismic core shadow as seen from InSight's location covers half the surface of Mars, including the majority of potentially active regions—e.g., Tharsis—possibly limiting the number of detectable marsquakes.

The core of a planet plays a prominent role because it governs many of the fundamental processes—from dynamo action and magnetic-field generation to mantle convection—that affect the surface through volcanic and tectonic activity and may influence the early climate through magnetic shielding of the atmosphere. The size of the martian core is of particular interest because of its notable impact on the planet's evolution, which differs from that of Earth primarily as a result of Mars' smaller size and, therefore, accelerated differentiation and core formation and cooling-off that resulted in a rigid-shell, one-plate planet (1, 2).

A small core with a radius between 1300 and 1600 km would be deficient in light elements and would accommodate a martian lower mantle similar to that of Earth, which is dominated by bridgmanite-structure silicates (3). A large core with a radius range between 1800 and 1900 km

would instead be enriched in light elements and exclude the presence of a phase transition equivalent to the 660-km discontinuity that marks the onset of Earth's lower mantle (4). It would exert a markedly different dynamic control over the martian mantle (5–8), with implications for an early martian dynamo (1) that could explain the observed highly magnetized crust in the southern highlands (9). Direct constraints on the core and deep interior of Mars, however, are scarce and limited to global geophysical measurements, including mass, moment of inertia, and tidal response (10, 11), in addition to geochemical data based on achondritic basaltic meteorites that originated from the surface of Mars (12–14). Collectively, these observations suggest a liquid core with a radius in the range of ~1700 to 1900 km (4, 8, 11, 15, 16). However, without additional observations, the range of potential martian core sizes encompasses a large enough range to allow for either the presence or the absence of a lower mantle.

The estimate of core size can be improved with the direct detection of core-interacting seismic phases, which constrain the core size of Earth and the Moon. Earth's core had been predicted in the late 18th century—on the basis of the recognition that the density of near-surface rocks is substantially lower than the average density of Earth (17)—but was not confirmed until global observations of earthquakes became possible (18). Subsequent seismic measurements led to unexpected discoveries in Earth's deep interior, such as the inner core (19) and deep mantle layering (20, 21). Similarly, the Apollo lunar seismic data (22) were used to establish the existence of a lunar core (23, 24). The detection of seismic waves reflected from the core stands not only to refine the

insights gained from studying the chemistry of the martian rocks, whose siderophile element depletion and isotopic signature point to a core-forming event early in Mars' history (25, 26), but also to considerably improve our understanding of the deep interior of Mars.

After a full martian year, the Interior Exploration using Seismic Investigations, Geodesy, and Heat Transport (InSight) mission (27) and its seismometer SEIS (28) have recorded a multitude of seismic events, which have been located and classified by the Marsquake Service (29–31). Of these, the low-frequency events with main energy below 1 Hz and waves traveling through the mantle can be used to characterize the crustal and mantle structure of Mars (32, 33).

To investigate the core of Mars, we analyzed seismic data from 11 low-frequency marsquakes. Six of them were found in a suitable distance range [27° to 38.5° (30)], with high enough signal-to-noise ratio (SNR) to identify potential core-reflected S waves (ScS waves) (Table 1). Because S waves cannot propagate in a fluid medium, the core-mantle boundary (CMB) acts as a polarization filter, reflecting horizontally polarized S waves (SH waves) back into the mantle, whereas vertically polarized S waves (SV) lose some energy as a result of S-to-P conversion. S waves reflected from the CMB are therefore expected to be predominantly horizontally polarized, with an azimuth orthogonal to the source-receiver direction. The events for which the direction could be determined from P- and S-wave polarization (S0173a and S0235b) appear to originate in the Cerberus Fossae graben system (29, 34), with backazimuths of 70° to 90°. The focal mechanisms inferred for these events confirmed normal faulting (35), resulting in relatively strong radiation of SH waves toward the core.

All low-frequency marsquakes show an S-wave coda dominated by receiver-side scattering (Fig. 1A) (31). Within this coda, the marsquake with the highest SNR observed so far (S0173a) shows a peak around 350 s after the main S-wave arrival. We used polarization filtering (36) to enhance signals that are linearly and horizontally polarized, as expected for ScS waves (Fig. 1A). After filtering, we observed matching signals for five other events (S0235b, S0407a, S0409d, S0484a, and S0325a) at a similar distance (Fig. 1B). To identify energy pulses that are consistent with ScS, we performed a slant stack (37) for the events, using predicted travel times in 5000 mantle models compatible with surface-reflected seismic body waves (32). The stack of energy in a 10-s time window (filtered between 0.3 and 0.8 Hz) around the predicted ScS arrival time shows the presence of a signal (Fig. 1C), at the time when a reflection from an ~1600-km depth

[1]Institute of Geophysics, ETH Zürich, Zürich, Switzerland. [2]Physik-Institut, University of Zürich, Zürich, Switzerland. [3]Jet Propulsion Laboratory, California Institute of Technology, Pasadena, CA, USA. [4]Université de Paris, Institut de physique du globe de Paris, CNRS, Paris, France. [5]Institut Supérieur de l'Aéronautique et de l'Espace SUPAERO, Toulouse, France. [6]Department of Geology, University of Maryland, College Park, MD, USA. [7]Geosciences Barcelona – CSIC, Barcelona, Spain. [8]Sorbonne Université, Muséum National d'Histoire Naturelle, UMR CNRS 7590, Institut de Minéralogie, de Physique des Matériaux et de Cosmochimie, IMPMC, Paris, France. [9]Department of Electrical and Electronic Engineering, Imperial College, London, UK. [10]Department of Earth, Planetary, and Space Sciences, University of California Los Angeles, Los Angeles, CA, USA. [11]School of Earth Sciences, University of Bristol, Bristol, UK. [12]DLR Institute of Planetary Research, Berlin, Germany. [13]Laboratoire de Planétologie et Géodynamique (LPG), UMR CNRS 6112, Université de Nantes, Université d'Angers, France. [14]Royal Observatory of Belgium, Brussels, Belgium. [15]Swiss Seismological Service (SED), ETH Zürich, Zürich, Switzerland. [16]Schmidt Institute of Physics of the Earth RAS, Moscow, Russia.
*Corresponding author. Email: simon.staehler@erdw.ethz.ch
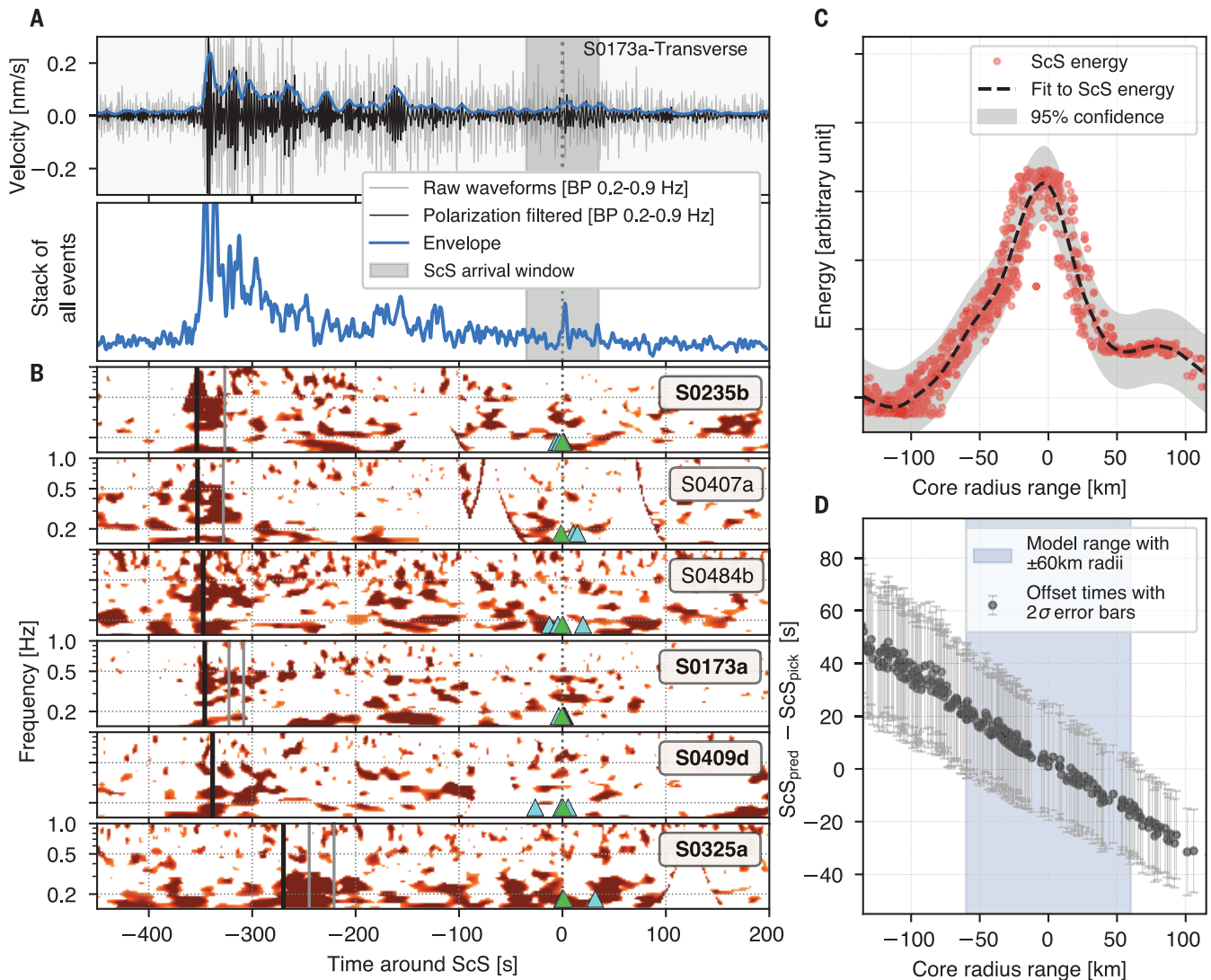
Fig. 1. Summary of data processing and identification of core-reflected S waves. (**A**) Seismogram and envelope of event S0173a before and after polarization filtering (top) and envelope stack for all six events (bottom). The individual event envelopes are shown in fig. S1-4 (*38*). (**B**) Polarization-filtered spectrograms for each of the six events considered here. Cyan triangles mark proposed *ScS* picks based on the processing methods described in the main text, and green triangles mark the final set of picks summarized in Table 1. Light gray lines mark *SS* and *SSS* picks from (*32*). All events show energy around the predicted arrival time of *ScS*, using a model from (*32*) with a core radius of 1830 km, in agreement with the *ScS* observation for S0173a shown in (A). Bold event labels (e.g., S0235b) indicate events with strong *ScS* energy. (**C**) Stacked energy in a 10-s time window around *ScS* as predicted for 5000 models from (*32*) with core radii centered around 1830. (**D**) Residual travel times of the models presented in (C) compared with the picks in (B), show that the *ScS* picks are able to constrain the core radius to within ±60 km (*80*).

interface is expected. This result is confirmed by a model-agnostic vespagram stack showing a low-slowness, steep incidence-angle arrival compatible with a deep reflector (*38*). To refine the arrival time estimate, the time window identified in the stacking was further examined using two independent methods: (i) manual picking in polarization-filtered filter banks to discriminate seismic phases and potential artifacts from instrument or wind and (ii) coda correlation using the *S* waveform as matching filter, assuming that the *S*-wave train has high similarity to *ScS* (*38*). This resulted in a set of picks for each event (Fig.

1D). The results from the two methods were compared with the event slant-stacks to remove misidentified signals and were consolidated into a single set of picks (Table 1).

Whereas the SNR of the *ScS* phases is around 2 or less, the signal is significant compared with the energy of the *S*-wave coda, wind noise, and known instrument artifacts (*38, 39*). From travel-time tables computed in seismic velocity models compatible with observations so far (*8, 32, 40*), no other seismic phase is predicted to arrive this late in the seismogram with similar move-out and polarization. Love waves traveling along the sur-

face would have similar polarization but arrive much earlier and show a large move-out and dispersion. Multiply-reflected body waves should also arrive earlier. We therefore interpreted this signal as an *S*-wave reflection from the CMB that, when using seismic velocity models from (*32*), corresponds to a core with a radius in the range 1770 to 1890 km. We also searched for other phases, such as core-reflected *P* waves (*PcP*), but were unable to find consistent arrivals. This was not unexpected because of the lower *P*-wave reflection coefficient at the CMB. A shear wave that is converted into a *P* wave at the CMB (*ScP*) is predicted to arrive 290 s after *P* for S0325a,
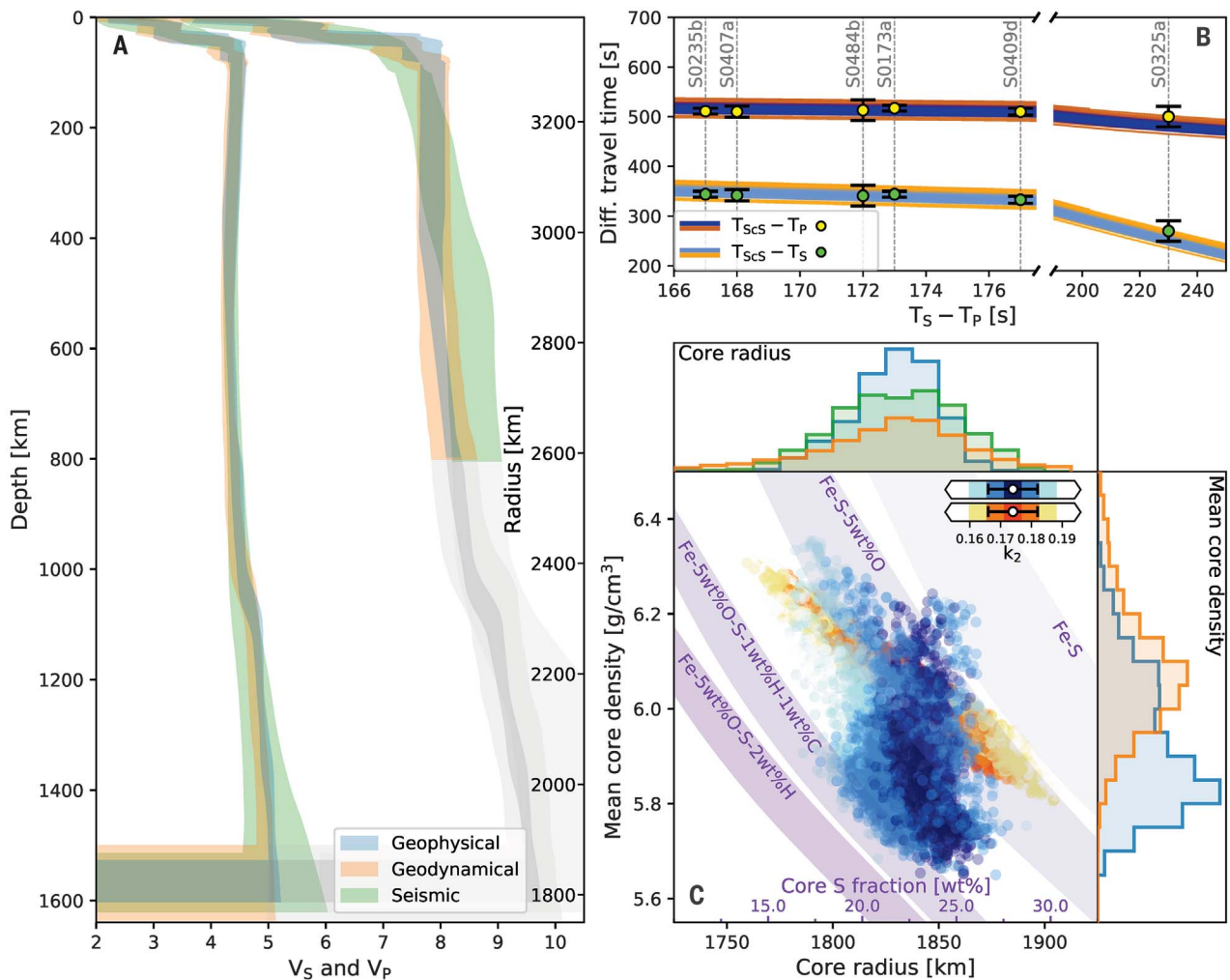
Fig. 2. Mars' mantle and core structure. (**A**) Inverted seismic wave velocity profiles (95% credible intervals) based on the three inversion methods defined here (see legend). The pale gray shaded area below 800-km depth for the *P*-wave velocity profiles indicates that no direct information is available for this region. (**B**) Differential body wave travel time misfits for all sampled models obtained from the geophysical (blue shades) and geodynamical (orange shades) inversions shown in (A). Yellow and green circles indicate the observations including error bars. A detailed version of the misfit plot is shown in fig. S9-1 (*38*). (**C**) Sampled core properties. The middle plot shows the mean core density versus core radius for the geophysical (blue) and geodynamical (orange) methods, whereas their marginal distributions are shown as histograms to the right and on the top. The seismic method only constrains core radius. The blue and orange models are color-coded according to their fit to the tidal response in the form of the observed degree-2 Love number k_2 (*11*), defined by the white circles and horizontal error bars. Relying on Fe-S models, the purple bands indicate the variation of core sulfur (S) content (purple axis) with mean core density for four different iron (Fe)–light element (S, O, H, and C) assemblages (*65–68*).

and we observed a weak phase by correlation analysis. This arrival is only 2 s after the identified *SSS* arrival reported in (*32*), so the peak, although consistent, is not used for inversion here.

The spectral character and the travel time of the deep-diving direct *S* wave for the most distant event (S0167b) located to date (*30, 32*) were consistent with and comparable to those of the *ScS* phase with similar travel times (fig. S6-1) (*38*). This supports the identification of the latter as a core reflection that has traversed the entire attenuating mantle. The attenuation-corrected power of the *ScS* phases is below that of the corresponding *S*-wave arrivals

by 10 to 20 dB. This value is slightly below the ray-theoretical prediction from geometrical spreading (fig. S6-2) (*38*), assuming full reflection of *SH* waves at the CMB, possibly because of scattering at other interfaces and three-dimensional structure. For four of the six events we investigated, (*32*) reports a second arrival within 20 s after the main *S* wave. We considered these secondary arrivals to be the depth phase (*sS*), resulting in marsquakes that occur in the depth range 20 to 35 km.
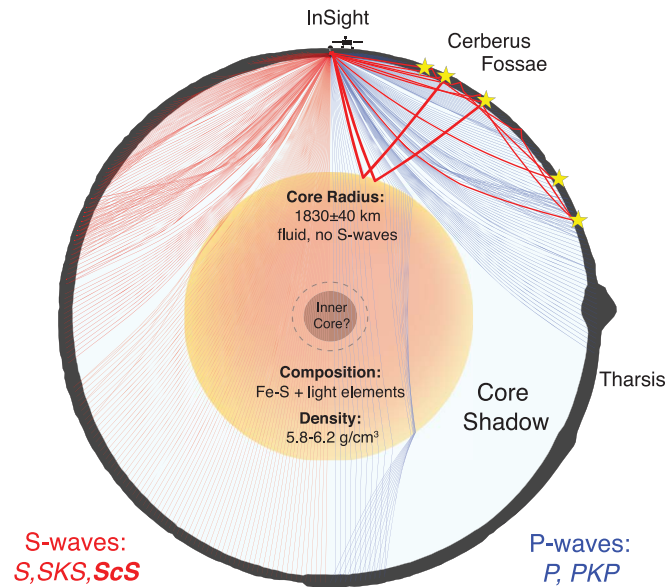
We inverted differential *ScS* travel times (Table 1) with respect to *P* together with the travel times of *S*, *PP*, *SS*, *PPP*, and *SSS*

from (*32*) and geodetic data in the form of the degree-2 Love number (*11*), mean density (*16*), and mean moment of inertia (*11*) for mantle *P*- and *S*-wave velocity and density, epicentral distance for all considered events, and radius and mean density of the core. We conducted three separate inversions that relied on a pure seismic parameterization and two mineralogically constrained inversions: a geodynamic (*41, 42*) and a geophysical parameterization (*4*). The seismic parameterization considers a layered model of Mars described by *P*- and *S*-wave velocity gradients, respectively, and does not use the geodetic data. The geodynamic parameterization depends on quantities that

influence the thermochemical evolution of the planet and accounts for 4.5 billion years of planetary evolution. The geophysical parameterization relies on a unified description of phase equilibria, seismic properties, and thermochemical parameters. The parameterizations (38) reflect, in going from seismic over geodynamic to geophysical parameterization, a decrease in the number of degrees of freedom, as the two latter parameterizations depend increasingly on mineral physics information and therefore better-resolved parameters. Because the mean density of the core depends on that of the mantle and therefore on the bulk mantle composition, we considered six different model martian compositions (12, 14, 43–47) as part of the geophysical inversion. To solve the inverse problem, we employed a stochastic algorithm (48) that samples models that fit the differential body wave travel times within uncertainties and are consistent with prior information (38).

We plotted the results from the joint inversion of the differential body wave travel times and the geophysical data (Fig. 2). The S-wave velocity profiles (Fig. 2A) we obtained from the three parameterizations were found to be in good agreement. More scatter exists in the P-wave velocity profiles, which reflects fewer P-wave observations, and structure is only constrained to 800-km depth (Fig. 2A). All parameterizations provide a good fit to the ScS-P travel time observations (Fig. 2B). Above 800-km depth, the velocity profiles are similar to those obtained by the upper mantle inversion (32), and below, the S-wave velocity profiles show a distinct increase around 1050-km depth, equivalent to the 410-km seismic discontinuity in Earth's mantle that marks the onset of the mantle transition zone, where the dominant upper mantle mineral olivine transforms to wadsleyite. The CMB occurs between 1520- and 1600-km depth, corresponding to CMB pressures of 18 to 19 GPa and temperatures in the range of ~1900 to 2000 K. These conditions are unfavorable for the stabilization of bridgmanite and imply that the lower mantle of Mars is mineralogically comparable to Earth's mantle transition zone. This means that a relatively dense and thermally insulating lower mantle is absent in Mars, which favors the development of an early thermally driven dynamo as a means of explaining crustal magnetism because of elevated core heat flux (1, 49, 50).

In agreement with geodetic observations that require a liquid core (10), the observation of ScS with substantial relative amplitudes compared with direct S waves rules out a solid outer core because reflection coefficients would be too small at a solid-solid interface [fig. S6-2 (38)]. The separate inversions converge on the same mean radius but show more spread in mean core density (Fig. 2C), which reflects the trade-off with mantle

density through bulk mantle composition (indicated by the blue circles in Fig. 1C). On the basis of the distributions, we estimate core radius to be 1830 ± 40 km, at the upper end of premission estimates (4, 8, 15, 16) that were based on an earlier and slightly lower degree-2 Love number [0.169 ± 0.006 (51)], and mean core density in the range 5.7 to 6.3 g/cm³. We also conducted separate inversions using the geodynamic method to consider the influence of individual datasets on the retrieved core properties (38). These inversions showed that the mean core radius changed from 1836 km (seismic data only) to 1815 km (geodetic data only), whereas the mean core density remained unchanged. To test the influence of the source depth, we fixed it to 50 km for all events—consistent with (29, 32)—and found that this would change the core radius to 1820 ± 40 km, within the above range.

Compositional constraints on the core typically derive from geochemical models coupled with metal-silicate partitioning and mass balance arguments (52–55) but depend on the assumed compositions of the building blocks (56, 57). Although sulfur is commonly considered the main light element (14, 44, 45, 55) because of its abundance in the mantle as determined from the martian meteorites (58) and its siderophile nature at the P-T-fO₂ conditions of the formation of Mars' core (59), additional light elements, including C, O, Si, N, and H, are all potentially viable candidates, as in Earth's core (60–63). Ni is also expected to be a core constituent based on meteorite compositions (64) and should make up 5 to 6 wt % (4). The purple-shaded areas in Fig. 2C indicate how the mean core density varies with S content in the Fe-S, Fe-S-O, Fe-S-O-H, and Fe-S-O-H-C systems, based on thermodynamic

Fig. 3. Schematic diagram of Mars' interior structure. The cross section depicts the core-induced shadow zone for seismic waves. The surface topography is a cut through the MOLA map (81) on a great circle arc from InSight through Olympus Mons. The S-wave shadow zone is minimal and probably filled by diffracted S waves (Sdiff), whereas the P-wave shadow zone is large and contains specifically the Tharsis region. The existence of an inner core cannot be determined by current data, and the seismic ray paths shown assume no inner core. Topography and InSight lander are exaggerated in scale.

Table 1. Consolidated differential travel times of S and ScS for the events used in this study. Magnitudes, M_w, are from the Marsquake Service catalog, version 6 (30), as defined by Böse et al. (82). Depth estimates are based on the identification of the depth phase sS (see the main text). The events are labeled by mission Sol of occurrence and sublabeled alphabetically for Sols with more than 1 event.

Event	tS-tP (s)	tScS-tP (s)	sigma(tScS)	Depth (km)	M_w
S0235b	167	511	3	24 ± 5	3.5
S0407a	168	510	10	25 ± 5	3.0
S0484b	172	513	20	33 ± 5	2.9
S0173a	173	512	3	24 ± 5	3.6
S0409d	177	510	5	25 ± 5	3.1
S0325a	230	500	20	30 ± 5	3.7

solution models constructed using experimental data (65–68). For a core composed of Fe and S, sulfur contents surpass 25 wt %, which is above the value of the sulfur-richest meteorites (EH chondrites) and in excess of what is deduced from geo- and cosmochemical models [<13 to 19 wt % (52, 55)]. To bring the S content in line with the cosmochemical constraints, additional light elements (e.g., C, O, and H) in the core are needed (fig. S11-1) (38). For geochemically defensible amounts of S, O, and H, the mean core density has to be >6 g/cm^3, which encompasses the upper end of our predictions (Fig. 2C). Because our core density estimate is tied to reasonable assumptions about the composition and temperature of the martian mantle, a higher mean core density is possible and requires less light elements as a result of a lower bulk mantle FeO content (46) or higher temperatures as seen in some geodynamic models (69). The influence of a lower bulk mantle FeO content on mean core density is reflected by the cloud of blue circles with a mean core density >6.1 g/cm^3 (Fig. 2C) that were obtained on the basis of the bulk mantle composition of (46). Thus, a lower bulk mantle FeO content seems to provide a better match than the canonical martian compositions with FeO contents exceeding 17 wt % (12, 14, 44, 45), which had also been found to be at odds with geophysical constraints (4, 57). As a preliminary observation, our results can be construed as pointing to an Fe-Ni core that is composed of, in order of abundance, S (10 to 15 wt %), O (<5 wt %), and H and C (<1 wt % level) (38). Although such O, H, and C contents represent upper limits, they serve to emphasize the need for light elements in Mars' core.

A chemical composition close to the eutectic (~15 wt % S in the Fe-FeS binary at the CMB conditions of Mars) likely prevented crystallization of a bottom-up inner core because of the temperatures (~1200 K) required to drop below the liquidus (70). This is compatible with the absence of a current martian geodynamo (71). Strong crustal remnant magnetization in the southern hemisphere of Mars (72) and observations of further magnetized units suggest a dynamo that was active between 4.5 and 3.7 billion years ago (9). The dynamo would have been thermally driven in the first few hundred million years (49, 50) and possibly followed by a compositionally driven dynamo that may resuscitate through FeO exsolution (73) or inner-core crystallization (71, 74, 75). This, however, depends critically on the light-element content and thermal state of the core.

As a consequence of the large core, the seismic core shadow on Mars (Fig. 3) commences at closer epicentral distances (94° to 98°) than on Earth [100° (76)]. This makes up half of the planet, including 33% of total extensional faults,

specifically 75% of those in terrain younger than 600 million years (77). For marsquakes in Tharsis, the region presumed to host most of the recent tectonic activity (78), direct P and S waves are therefore unobservable, and this may result in an underestimation of the global seismic activity of Mars as seen from InSight's location (27).

The differentiation of Mars into a primordial crust, mantle, and core is likely the result of early magma ocean crystallization and solidification that could potentially result in compositional stratification of the mantle (69, 79). There is, however, no direct evidence for this on the basis of current observations. Continued analysis using marsquakes observed during the extended mission will be required to delve into the question of deep mantle layering. To determine the compressional wave speeds of the core itself and further refine light-element content, an unequivocal observation of an event beyond the core shadow, with clear core-crossing phases like PKP or SKS, will be necessary. This would allow us to employ velocity-density systematics (61) as a means of gaining further insight into the total light-element content of the core. In the interim, the new martian seismic data and models presented here provide a wealth of new insights into the interior structure of Mars, which contain the clues needed to unravel the planetary building blocks (57); the physical and chemical conditions during assembly (52); and the chronology of crust, mantle, and core formation (25).

REFERENCES AND NOTES

1. D. J. Stevenson, *Nature* **412**, 214–219 (2001).
2. M. T. Zuber et al., *Science* **287**, 1788–1793 (2000).
3. C. M. Bertka, Y. Fei, *Earth Planet. Sci. Lett.* **157**, 79–88 (1998).
4. A. Khan et al., *J. Geophys. Res. Planets* **123**, 575–611 (2018).
5. D. Breuer, D. A. Yuen, T. Spohn, *Earth Planet. Sci. Lett.* **148**, 457–469 (1997).
6. P. van Thienen, N. J. Vlaar, A. P. van den Berg, *Phys. Earth Planet. Inter.* **142**, 61–74 (2004).
7. T. Ruedas, P. J. Tackley, S. C. Solomon, *Phys. Earth Planet. Inter.* **216**, 32–58 (2013).
8. S. E. Smrekar et al., *Space Sci. Rev.* **215**, 3 (2019).
9. A. Mittelholz, C. L. Johnson, J. M. Feinberg, B. Langlais, R. J. Phillips, *Sci. Adv.* **6**, eaba0513 (2020).
10. C. F. Yoder, A. S. Konopliv, D. N. Yuan, E. M. Standish, W. M. Folkner, *Science* **300**, 299–303 (2003).
11. A. S. Konopliv et al., *Geophys. Res. Lett.* **47**, e2020GL090568 (2020).
12. G. Dreibus, H. Wänke, in *Proceedings of the 27th International Geological Congress*, vol. 11 (1984), pp. 1–20.
13. H. Y. McSween Jr., K. Keil, *Geochim. Cosmochim. Acta* **64**, 2155–2166 (2000).
14. G. J. Taylor, *Geochemistry* **73**, 401–420 (2013).
15. A. Bagheri, A. Khan, A. Al-Attar, O. Crawford, D. Giardini, *J. Geophys. Res. Planets* **124**, 2703–2727 (2019).
16. A. Rivoldini, T. Van Hoolst, O. Verhoeven, A. Mocquet, V. Dehant, *Icarus* **213**, 451–472 (2011).
17. C. Hutton, *Phil. Trans. R. Soc.* **68**, 689–788 (1778).
18. R. D. Oldham, *Q. J. Geol. Soc.* **62**, 456–475 (1906).
19. I. Lehmann, *Séismol. Internat. Strasbourg Publ. Bur. Centr. Sci.* **14**, 87–115 (1936).
20. K. E. Bullen, *Phys. Chem. Earth* **1**, 68–93 (1956).
21. C. G. Dahm, *Eos Trans. AGU* **15**, 80–83 (1934).
22. G. Latham et al., *Science* **174**, 687–692 (1971).
23. R. F. Garcia, J. Gagnepain-Beyneix, S. Chevrot, P. Lognonné, *Phys. Earth Planet. Inter.* **188**, 96–113 (2011).
24. R. C. Weber, P.-Y. Lin, E. J. Garnero, Q. Williams, P. Lognonné, *Science* **331**, 309–312 (2011).
25. N. Dauphas, A. Pourmand, *Nature* **473**, 489–492 (2011).
26. K. Mezger, V. Debaille, T. Kleine, *Space Sci. Rev.* **174**, 27–48 (2013).
27. W. B. Banerdt et al., *Nat. Geosci.* **13**, 183–189 (2020).
28. P. Lognonné et al., *Space Sci. Rev.* **215**, 12–12 (2019).
29. D. Giardini et al., *Nat. Geosci.* **13**, 205–212 (2020).
30. InSight Marsquake Service, Mars Seismic Catalogue, InSight Mission; V6 2021-04-01 (ETHZ, IPGP, JPL, ICL, MPS, Univ. Bristol, 2021); https://doi.org/10.12686/a11.
31. P. Lognonné et al., *Nat. Geosci.* **13**, 213–220 (2020).
32. A. Khan et al., *Science* **373**, 434–438 (2021).
33. B. Knapmeyer-Endrun et al., *Science* **373**, 438–443 (2021).
34. J. Taylor, N. A. Teanby, J. Wookey, *J. Geophys. Res. Planets* **118**, 2570–2581 (2013).
35. N. Brinkman et al., *J. Geophys. Res. Planets* **126**, e2020JE006546 (2021).
36. M. Schimmel, J. Gallart, *Bull. Seismol. Soc. Am.* **94**, 1016–1035 (2004).
37. P. S. Schultz, J. F. Claerbout, *Geophysics* **43**, 691–714 (1978).
38. Materials and methods are available as supplementary materials.
39. J.-R. Scholz et al., *Earth Space Sci.* **7**, 1–31 (2020).
40. A.-C. Plesa et al., *J. Geophys. Res. Planets* **126**, e2020JE00675514 (2021).
41. M. Drilleau, H. Samuel, A. Rivoldini, M. Panning, P. Lognonné, *Geophys. J. Int.* **226**, 1615–1644 (2021).
42. H. Samuel, P. Lognonné, M. Panning, V. Lainey, *Nature* **569**, 523–527 (2019).
43. A. Khan, J. A. D. Connolly, *J. Geophys. Res.* **113**, E07003 (2008).
44. K. Lodders, B. Fegley Jr., *Icarus* **126**, 373–394 (1997).
45. C. Sanloup, A. Jambon, P. Gillet, *Phys. Earth Planet. Inter.* **112**, 43–54 (1999).
46. T. Yoshizaki, W. F. McDonough, *Geochim. Cosmochim. Acta* **273**, 137–162 (2020).
47. C. B. Agee, D. S. Draper, *Earth Planet. Sci. Lett.* **224**, 415–429 (2004).
48. K. Mosegaard, A. Tarantola, *J. Geophys. Res.* **100**, 12431–12447 (1995).
49. D. Breuer, T. Spohn, *J. Geophys. Res.* **108**, 5072 (2003).
50. J.-P. Williams, F. Nimmo, *Geology* **32**, 97–100 (2004).
51. A. S. Konopliv, R. S. Park, W. M. Folkner, *Icarus* **274**, 253–260 (2016).
52. M. C. Brennan, R. A. Fischer, J. C. E. Irving, *Earth Planet. Sci. Lett.* **530**, 115923 (2020).
53. K. Righter, N. L. Chabot, *Meteorit. Planet. Sci.* **46**, 157–176 (2011).
54. D. C. Rubie et al., *Icarus* **248**, 89–108 (2015).
55. E. S. Steenstra, W. van Westrenen, *Icarus* **315**, 69–78 (2018).
56. C. Fitoussi, B. Bourdon, X. Wang, *Earth Planet. Sci. Lett.* **434**, 151–160 (2016).
57. C. Liebske, A. Khan, *Icarus* **322**, 121–134 (2019).
58. G. Dreibus, H. Wänke, *Meteoritics* **20**, 367–381 (1985).
59. N. Rai, W. van Westrenen, *J. Geophys. Res. Planets* **118**, 1195–1203 (2013).
60. J. Badro, J. P. Brodholt, H. Piet, J. Siebert, F. J. Ryerson, *Proc. Natl. Acad. Sci. U.S.A.* **112**, 12310–12314 (2015).
61. F. Birch, *J. Geophys. Res.* **69**, 4377–4388 (1964).
62. J.-P. Poirier, *Phys. Earth Planet. Inter.* **85**, 319–337 (1994).
63. V. N. Zharkov, *Sol. Syst. Res.* **30**, 456 (1996).
64. A. E. Ringwood, *Geochem. J.* **11**, 111–135 (1977).
65. J. V. Badding, H. K. Mao, R. J. Hemley, in *High-Pressure Research: Application to Earth and Planetary Sciences* (American Geophysical Union, 1992), pp. 363–371.
66. T. Komabayashi, *J. Geophys. Res. Solid Earth* **119**, 4164–4177 (2014).
67. G. Morard et al., *Am. Mineral.* **103**, 1770–1779 (2018).
68. H. Terasaki et al., *J. Geophys. Res. Planets* **124**, 2272–2293 (2019).
69. L. T. Elkins-Tanton, E. M. Parmentier, P. C. Hess, *Meteorit. Planet. Sci.* **38**, 1753–1771 (2003).
70. Y. Mori et al., *Earth Planet. Sci. Lett.* **464**, 135–141 (2017).
71. A. J. Stewart, M. W. Schmidt, W. van Westrenen, C. Liebske, *Science* **316**, 1323–1325 (2007).
72. M. H. Acuña et al., *Science* **284**, 790–793 (1999).
73. K. Tsuno, E. Ohtani, H. Terasaki, *Phys. Earth Planet. Inter.* **160**, 75–85 (2007).
74. D. Breuer, W. B. Moore, in *Treatise on Geophysics*, G. Schubert, Ed. (Elsevier, ed. 2, 2015), pp. 255–305.
75. D. J. Hemingway, P. E. Driscoll, *J. Geophys. Res. Planets* **126**, e2020JE006663 (2021).
76. B. L. N. Kennett, E. R. Engdahl, *Geophys. J. Int.* **105**, 429–465 (1991).
77. M. Knapmeyer et al., *J. Geophys. Res.* **111**, E11006 (2006).
78. R. C. Anderson et al., *J. Geophys. Res.* **106**, 20563–20585 (2001).

79. H. Samuel et al., J. Geophys. Res. Planets **126**, e2020JE006613 (2021).
80. A. G. Marusiak, N. C. Schmerr, M. E. Banks, I. J. Daubar, Icarus **335**, 113396 (2020).
81. D. E. Smith et al., J. Geophys. Res. **106**, 23689–23722 (2001).
82. M. Böse et al., Bull. Seismol. Soc. Am., 10.1785/0120210045 (2021).
83. J. D. Hunter, Comput. Sci. Eng. **9**, 90–95 (2007).
84. L. Krischer et al., Comput. Sci. Discov. **8**, 014003 (2015).
85. C. R. Harris et al., Nature **585**, 357–362 (2020).
86. P. Virtanen et al., Nat. Methods **17**, 261–272 (2020).
87. InSight Mars SEIS Data Service, SEIS raw data, Insight Mission (IPGP, JPL, CNES, ETHZ, ICL, MPS, ISAE-Supaero, LPG, MFSC, 2019); https://doi.org/10.18715/SEIS.INSIGHT.XB_2016.
88. S. C. Stähler, M. Drilleau, A. C. Duran, A. Khan, H. Samuel, Interior Models of Mars from inversion of seismic body waves (2021); https://doi.org/10.18715/IPGP.2021.kpmqrnz8.

SUPPLEMENTARY MATERIALS

science.sciencemag.org/content/373/6553/443/suppl/DC1
Materials and Methods
Figs. S1-1 to S11-1
Tables S0 to S8-3
References (89–125)

Science

Seismic detection of the martian core

Simon C. StählerAmir KhanW. Bruce BanerdtPhilippe LognonnéDomenico GiardiniSavas CeylanMélanie DrilleauA. Cecilia DuranRaphaël F. GarciaQuancheng HuangDoyeon KimVedran LekicHenri SamuelMartin SchimmelNicholas SchmerrDavid SollbergerÉléonore StutzmannZongbo XuDaniele AntonangeliConstantinos CharalambousPaul M. DavisJessica C. E. IrvingTaichi KawamuraMartin KnapmeyerRoss MaguireAngela G. MarusiakMark P. PanningClément PerrinAna-Catalina PlesaAttilio RivoldiniCédric SchmelzbachGéraldine ZenhäusernÉric BeuclerJohn ClintonNikolaj DahmenMartin van DrielTamara GudkovaAnna HorlestonW. Thomas PikeMatthieu PlasmanSuzanne E. Smrekar

Single seismometer structure

Because of the lack of direct seismic observations, the interior structure of Mars has been a mystery. Khan *et al.*, Knapmeyer-Endrun *et al.*, and Stähler *et al.* used recently detected marsquakes from the seismometer deployed during the InSight mission to map the interior of Mars (see the Perspective by Cottaar and Koelemeijer). Mars likely has a 24- to 72-kilometer-thick crust with a very deep lithosphere close to 500 kilometers. Similar to the Earth, a low-velocity layer probably exists beneath the lithosphere. The crust of Mars is likely highly enriched in radioactive elements that help to heat this layer at the expense of the interior. The core of Mars is liquid and large, #1830 kilometers, which means that the mantle has only one rocky layer rather than two like the Earth has. These results provide a preliminary structure of Mars that helps to constrain the different theories explaining the chemistry and internal dynamics of the planet.

Science, abf2966, abf8966, abi7730, this issue p. 434, p. 438, p. 443 see also abj8914, p. 388

View the article online
https://www.science.org/doi/10.1126/science.abi7730
Permissions
https://www.science.org/help/reprints-and-permissions